NANO LETTERS

pubs.acs.org/NanoLett

Letter

Polymer-like Inorganic Double Helical van der Waals Semiconductor

Jiangbin Wu,*,# Nan Wang,# Ya-Ru Xie, Hefei Liu, Xinghao Huang, Xin Cong, Hung-Yu Chen, Jiahui Ma, Fanxin Liu, Hangbo Zhao, Jun Zhang, Ping-Heng Tan, and Han Wang*

Cite This: *Nano Lett.* 2022, 22, 9054–9061

Read Online

ACCESS | Metrics & More | Article Recommendations | Supporting Information

ABSTRACT: In high-performance flexible and stretchable electronic devices, conventional inorganic semiconductors made of rigid and brittle materials typically need to be configured into geometrically deformable formats and integrated with elastomeric substrates, which leads to challenges in scaling down device dimensions and complexities in device fabrication and integration. Here we report the extraordinary mechanical properties of the newly discovered inorganic double helical semiconductor tin indium phosphate. This spiral-shape double helical crystal shows the lowest Young's modulus (13.6 GPa) among all known stable inorganic materials. The large elastic (>27%) and plastic (>60%) bending strains are also observed and attributed to the easy slippage between neighboring double helices that are coupled through van der Waals interactions, leading to the high flexibility and deformability among known semiconducting materials. The results advance the fundamental understanding of the unique polymer-like mechanical properties and lay the foundation for their potential applications in flexible electronics and nanomechanics disciplines.

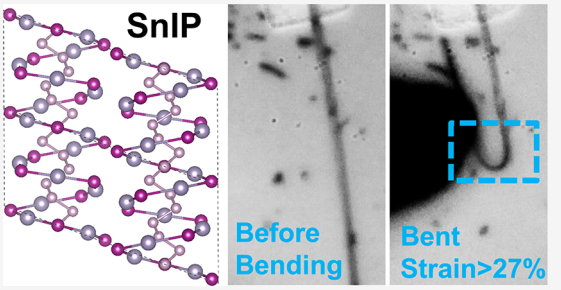

KEYWORDS: *Inorganic double helix, Young's modulus, Deformability, van der Waals crystal, SnIP*

Compared with organic semiconductors, inorganic semiconductors have significantly higher field-effect mobilities and long-term stability, which are desirable for high-performance flexible and stretchable electronics.[1,2] However, due to their high Young's modulus, small yield strain, and fracture limit, inorganic semiconductors typically require large deformation forces and have small elastic deformation ranges. Such intrinsically nonbendable and nonstretchable characteristics of inorganic semiconductors significantly limit their applications in flexible and stretchable electronics where large deformations are involved. To overcome these limitations, several approaches have been presented. For example, the size-dependent mechanical properties of one-dimensional (1D) semiconductors such as silicon nanowires were utilized to achieve enhanced flexibility as compared to their large-scale counterparts.[3−5] Moreover, large numbers of nanowires were used in a single device to make sure the performance would not degrade quickly under repeated bending or stretching.[4,6] Another approach is leveraging structural designs to form nanoscale semiconductor thin films into out-of-plane buckled structures[7] or in-plane serpentine structures[8,9] to accommodate overall structure deformations while avoiding substantial strains in the semiconductor material itself. However, those approaches yield limited flexibility and stretchability and are challenging to scale down key device dimensions below tens or hundreds of micrometers,[6,9] limiting their use in devices with increasing spatial resolution and integration density. Therefore, inorganic semiconductors with polymer-like mechanical properties, such as low Young's modulus and high intrinsic stretchability, are highly desirable for the next-generation flexible and stretchable electronic devices.

Double helical structure has always been of central interest to a broad range of scientific and engineering disciplines from the architectural marvel of Bramante Staircase in the Vatican City to the molecular structure of deoxyribonucleic acid (DNA).[10−13] In crystal, the atomic double helical structure would provide a lower Young's modulus and higher elasticity. Unlike the double helical nanostructures formed through the physical winding of carbon nanotube, nanowires, and 2D materials,[14−18] such double-helical crystals are expected to consist of atomic-scale double helices orderly arranged in a highly crystalline manner. Each individual double helix unit in the crystal lattice would consist of two atomic spiral strands with identical pitches intertwined about a common axis at the fundamental atomic scale. However, inorganic solid state crystals with analogous double helical atomic lattices have remained largely unexplored by the physical science community.[19,20]

In this work, we study the mechanical properties (including Young's modulus, flexibility, and deformability) of a semi-

Received: August 29, 2022
Revised: October 27, 2022
Published: November 2, 2022

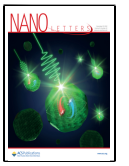

https://doi.org/10.1021/acs.nanolett.2c03394
Nano Lett. 2022, 22, 9054–9061

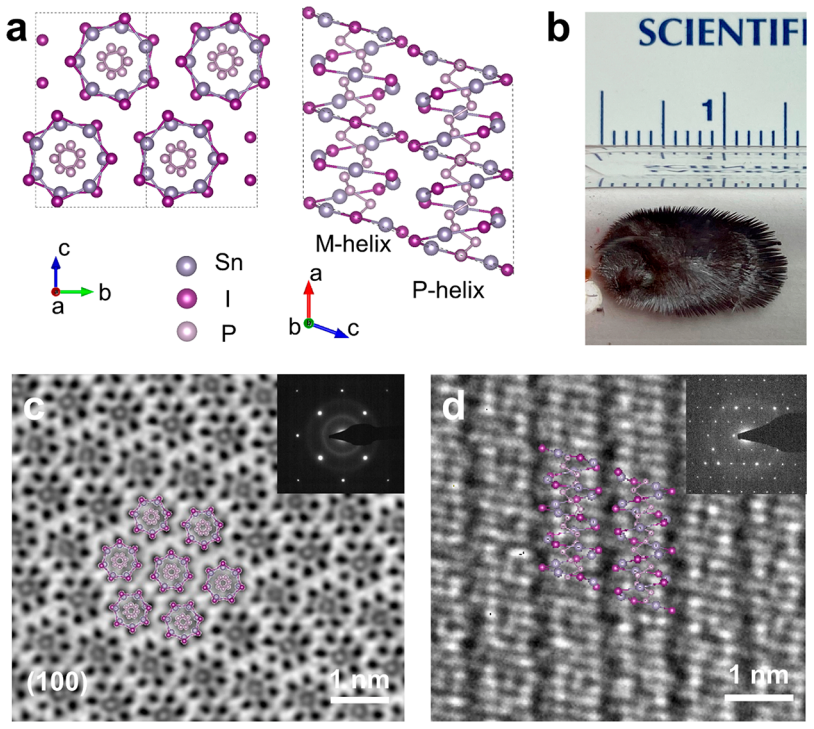

Figure 1. SnIP crystal structure and characterization. (a) Atomic structure of the SnIP crystal viewed along the *a*-axis (left panel) and *b*-axis (right panel), respectively. (b) Optical image of the as-grown SnIP in a sealed quartz tube. (c) Atomic resolution bright field HR-STEM image of the (100) plane in the SnIP crystal. (d) Dark field HR-STEM image along the [100] direction of the SnIP crystal. The insets in (c) and (d) show the corresponding electron diffraction patterns, respectively.

conducting, carbon-free inorganic double helical van der Waals crystal tin indium phosphate (SnIP).[21] The Young's modulus (E) of SnIP along the double helical strand axis is proved to be lower than any other existing experimentally tested inorganic crystals and even lower than that of many organic materials, according to both the nanomechanical bending test and the Brillouin scattering spectroscopy measurement. Then, a large elastic bending strain (>27%) is observed, resulting in the high flexibility of SnIP comparable to polymer. Furthermore, out of the yield strain limit, a high plastic bend strain (>60%) is also recorded, leading to a high deformability comparable to metal. Density-functional theory (DFT) calculation reveals that the low slipping energy between van der Waals coupled neighboring double helices is the reason for high flexibility and deformability.

The bulk SnIP crystal belongs to the C_{2h} space group, with lattice parameters of a = 0.79 nm, b = 0.98 nm, c = 1.84 nm, and β = 110.1° (Figure 1a). Two substructures (strands) of different elemental compositions (an inner helical chain consisting of phosphorus atoms (inner strand) and an outer helical chain consisting of alternating tin and iodide atoms (outer strand)) form the SnIP double helix. The inner and outer strands of an individual double helix have the same chirality, i.e., either left (M-helix) or right-handed (P-helix). Each two winding cycles of the intertwined strand pair contain seven SnIP units leading to a 7/2 helix. In the most thermodynamically stable form, alternating M and P helices bind together through van der Waals (vdW) interaction to form the bulk crystal lattice structure. The center-to-center distance between neighboring double helices is 0.98 nm. Thus, there are 42 atoms in each unit cell of the bulk SnIP crystal lattice. Optical image of the as-grown SnIP bulk crystal is shown in Figure 1b. Due to the vdW interaction between the neighboring double helices, the SnIP material can be exfoliated into nanowire-shape crystals on the SiO_2/Si substrate (see Method in Supporting Information).[22−24] The optical micrograph and the scanning electron microscopy (SEM) image of typical SnIP crystals exfoliated into the nanowire form are shown in Figure S1 of the Supporting Information. The typical cross sections of the exfoliated nanowires are close to a rectangle with width in the range of 0.1−1.5 μm, as shown in the SEM and energy-dispersive X-ray spectroscopy (EDS) images (Figure S2 of the Supporting Information). Figure 1c shows the bright field high resolution scanning transmission electron microscopy (HR-STEM) image of the SnIP crystal perpendicular to the [100] direction. As shown in Figure 1c, the bulk SnIP crystal lattice is revealed with both the inner and outer strands of each individual double helix clearly observed as heptagonal rings in this cross-sectional view. Figure 1d presents the dark field HR-STEM image along the [100] direction of the SnIP crystal, which shows the double helical strands arranged in parallel along the *a*-axis. The corresponding selected-area electron diffraction patterns are also provided in the insets of Figures 1c,d, which confirm the pseudohexagonal arrangement of the double helical units perpendicular to the *a*-axis and their parallel arrangement along the *a*-axis, respectively.

An atomic force microscope (AFM)-based nanomechanical bending test[25,26] was employed to measure the Young's modulus of SnIP crystals along the *a*-axis. Circular openings with depth of 300 nm were first etched in the SiO_2/Si substrate. The nanowire-shape SnIP crystals were then suspended across these openings. To improve the measurement accuracy, metal (Au/Cr) pads were deposited at both ends of the SnIP nanowire as the anchoring points (see

https://doi.org/10.1021/acs.nanolett.2c03394
Nano Lett. 2022, 22, 9054−9061

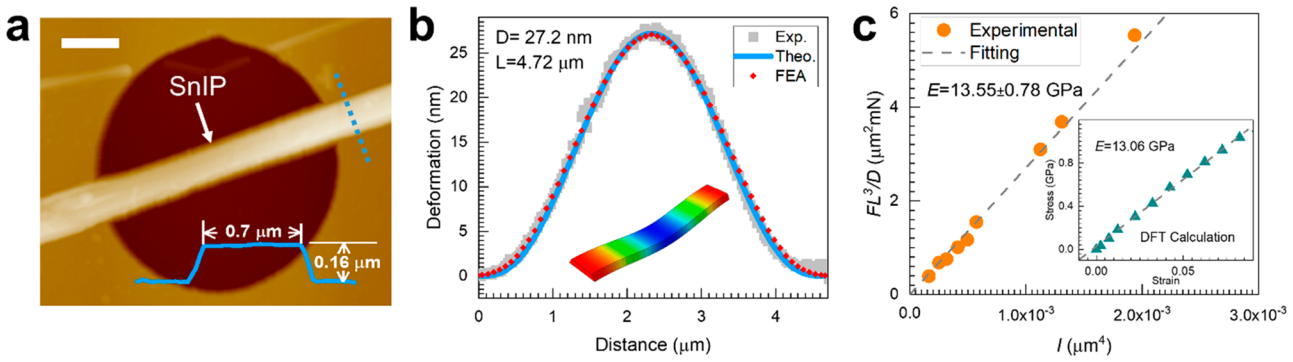

Figure 2. SnIP Young's modulus from nanomechanical bending test. (a) AFM height mapping of the suspended SnIP nanowire. The inset shows the height profile of the nanowire along the blue dashed line. The scale bar is 1 μm. (b) Deformation−distance curves obtained from the experimental measurement, analytical theory, and FEA, respectively, for the sample shown in (a). The inset is a simulated three-dimensional image of the deformed sample in (a) with deformation scaled by 10× for visualization. (c) Relationship between the FL^3/D and moment of inertia (I) of nine different samples. Inset: theoretical tensile stress−strain relationship of the SnIP crystal along the a-axis calculated using DFT.

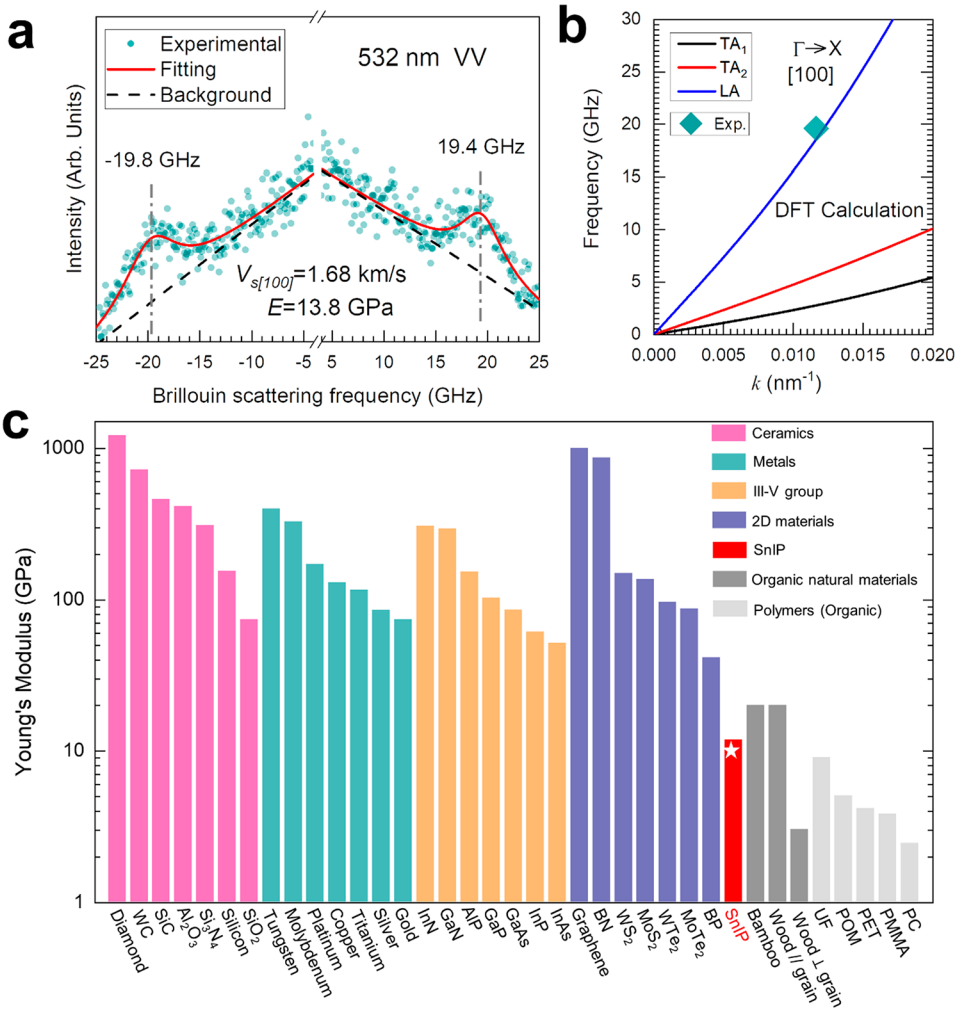

Figure 3. SnIP Young's modulus from Brillion scattering spectroscopy measurement. (a) Brillouin scattering spectra of SnIP along the a-axis. (b) Acoustic phonon dispersion relations along the a-axis calculated using DFT. One longitudinal acoustic (LA) and two transverse acoustic (TA_1 and TA_2) phonon branches are shown. (c) Benchmark of Young's modulus among different material classes.

Method in Supporting Information for details), as shown in the AFM height image in Figure 2a.

During the nanomechanical bending test, the AFM probe is scanned along the SnIP nanowire. At each measurement position, the force applied by the probe (F) is kept constant and the resulting deformation (δ) at the point of contact is recorded. Based on elastic beam-bending theory, the deformation δ as a function of the distance (d) for beams under point load with both ends fixed should follow[27] $\delta(d) = 64d^3(L-d)^3D/L^6$, where L is the effective suspended length of the SnIP nanowire, D is the deformation at the center of the SnIP nanowire when the load is applied at the same location,

https://doi.org/10.1021/acs.nanolett.2c03394
Nano Lett. 2022, 22, 9054−9061

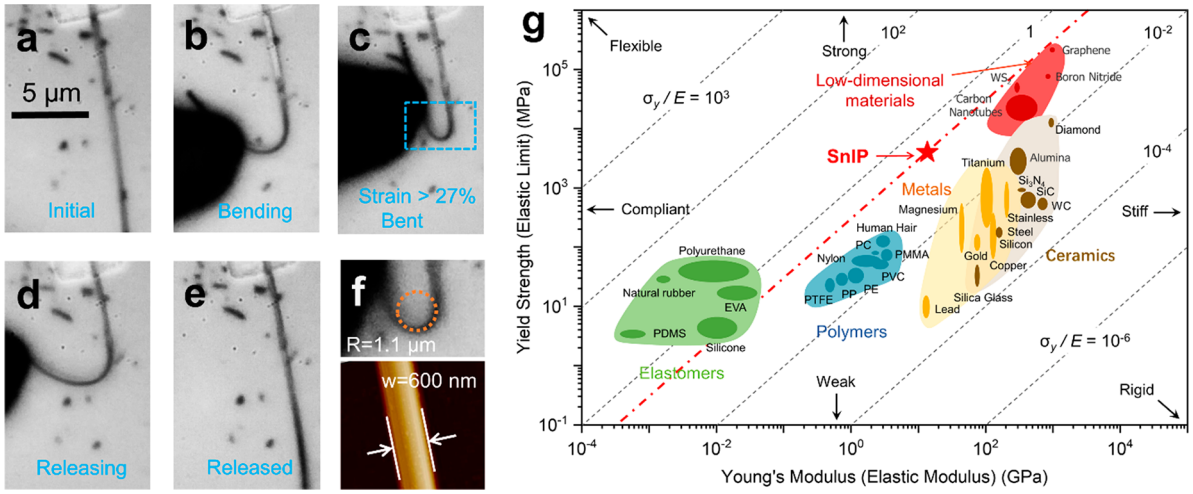

Figure 4. Flexibility of the SnIP nanowire. (a–e) Optical images recorded at the different stages of the bending test showing full recovery to the initial configuration after release. The bending was performed using a micromanipulated probe tip. One end of the nanowire was anchored with a metal pad. (f) Top panel: zoomed-in optical image of the bent SnIP nanowire marked with the dashed line in (a)–(e). Bottom panel: AFM height map of the same SnIP nanowire as in the top panel. (g) Figure of merit for flexibility of materials.

and d is the distance from the effective anchoring point reference position to the position of the probe where the force is applied (see Method in Supporting Information for details). As shown in Figure 2b, the experimental results are in excellent agreement with the theoretical model prediction. Moreover, the Young's modulus E along the a-axis can be extracted based on $E = FL^3/(192ID)$.[27] The area moment of inertia (I) of the SnIP nanowire under vertical loading is calculated based on its cross-sectional profile experimentally obtained using the AFM as shown in the inset of Figure 2a. To further validate the experiment results, Finite element analysis (FEA) is used to simulate the displacement as a function of the distance $\delta(d)$ based on the extracted E. The simulated probe-response scenario bears closer similarity to the actual experimental configuration (see Methods in Supporting Information) and hence is expected to provide better accuracy as compared to the analytical model. The simulation matches well with the experimental results and agrees with the analytical results as shown in Figure 2b. A representative nanowire deformation calculated by FEA with applied load at the center is shown in Figure S3 of the Supporting Information. To further improve the accuracy of the Young's modulus measurement, a total of nine samples with various measurement configurations, especially the L (varying from 2 to 10 μm), are measured. The average value of the Young's modulus E obtained across all the measured samples is 13.55 ± 0.78 GPa (Figure 3c). The small residual error of the obtained value also validates the reliability of the measurement. Moreover, F is chosen to be relatively small (about hundreds of nN) during all the measurements to ensure that the strain in the SnIP nanowire (ε) is well below the elastic limit. Using the sample in Figure 2b as an example, when the force is applied at the center, the bending strain can be estimated using the analytical expression $\varepsilon_{max} \approx \frac{Mt}{2EI}$, where $M = \frac{FL}{8}$ is the bending moment at the point of load and t is the thickness of the nanowire.[27] The calculated ε_{max} = 0.23% agrees with the FEA simulation (0.23%) and is also well within the elastic regime (<9%) as predicted by DFT calculations[28−30] (to be discussed later). The theoretical tensile stress (σ)−strain relationship of SnIP along the a-axis as calculated by DFT is shown in the inset of Figure 2c. The DFT calculation predicts a Young's modulus of $E \sim 13.06$ GPa for the SnIP crystal as obtained by fitting the initial linear regime (up to 9% here) of the calculated σ–ε curve, which is in close agreement with the nanomechanical bending test results.

To further obtain the Young's modulus of SnIP at a more fundamental level, the Brillouin scattering spectroscopy[31] measurement is carried out to probe the photon−phonon interactions in the SnIP crystals. As shown in Figure 3a, under the VV polarization configuration (the polarizations of both the incident and scattered light are fixed along the a-axis of the SnIP crystal), a pair of peaks are observed around ±19.6 GHz with 532 nm wavelength incident laser, corresponding to the scattering of light by the longitudinal acoustic (LA) phonon along the a-axis of the SnIP crystal.[32] Thus, the velocity of sound along the a-axis ([100] direction) can be extracted[33] as $V_{s[100]} = f\lambda/[2n\sin(\theta/2)]$, where f is the Brillouin scattering frequency, λ is wavelength of the incident laser light, n is the refractive index along the a-axis of the SnIP crystal, and θ is the angle between the incident and scattered beams. Here, we adopt n = 3.1 based on the DFT calculation, and θ =180° due to the backscattering geometry, which results in $V_{s[100]}$ = 1.68 km/s. The Young's modulus can hence be obtained as[34] $E = \rho V_{s[100]}^2$ = 13.8 GPa, where ρ = 4.77 g/cm^3 is the mass density of SnIP. This result is consistent with the Young's modulus value obtained using the nanomechanical bending test. In solid state crystals, the velocity of sound is equivalent to the slope of the dispersion curve for the corresponding acoustic phonons. Figure 3b shows the acoustic phonon dispersion relations along the Γ to X direction ([100]) as calculated by DFT. For small values of the wave vector (k), the acoustic phonon dispersions are approximately linear and the experimental results from the Brillouin scattering match well onto the calculated dispersion curve for the longitudinal acoustic phonon along the [100] direction as indicated in Figure 3b. Here, we would also like to note that previous work reported the experimentally measured Young's modulus in SnIP to be well over 190 GPa due to possible inaccuracy in the experiment or sample degradation, even though the same work also mentioned that the theoretical value of SnIP bulk modulus should be around 14.9 GPa.[35]

https://doi.org/10.1021/acs.nanolett.2c03394
Nano Lett. 2022, 22, 9054−9061

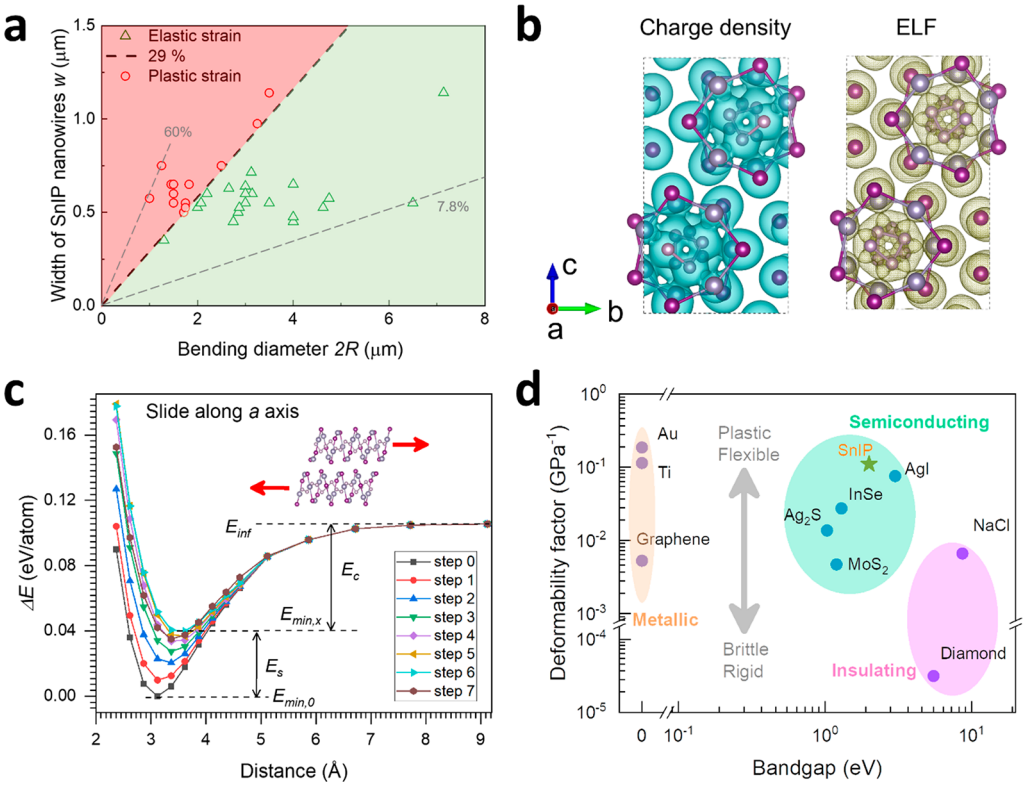

Figure 5. Deformability of the SnIP nanowire. (a) Bending strains measured in 35 SnIP nanowire samples. (b) Calculated charge density and electron localization function (ELF) of the SnIP crystal. (c) Energy variation as a function of the interdouble-helix distance during the slipping along the *a*-axis. (d) Benchmark of the deformability in materials of different electronic bandgaps.

Comparing the Young's modulus of the SnIP crystal with other air-stable materials, its E along the *a*-axis, which has been independently confirmed by both the nanomechanical bending test and the Brillouin scattering measurement, is significantly smaller than any other known inorganic materials, including all the ceramics, metals, III−V compounds, as well as low-dimensional materials such as carbon nanotube, nanowire crystals, and all the known 2D materials. The Young's modulus of SnIP is even comparable to or lower than many organic materials such as bamboo, wood, and polyoxymethylene (POM),[36] as shown in Figure 3c. Here, we attribute the ultralow Young's modulus of SnIP to the unique double helix lattice structure, in which the strong interatomic bonding between the P atoms in the inner strands and between the Sn and I atoms in the outer strands are along the tangential direction of the helices, leading to the significantly relaxed interactions along the *a*-axis, analogous to atomic-scale mechanical springs.

To further characterize the flexibility of the material, SnIP nanowire crystals were bent into U-shape by fixing one end of the nanowires and moving the other end using a micromanipulated probe tip.[37] In this test, one end of the SnIP nanowire was anchored in place and a micromanipulated probe tip was used to bend the nanowire. Figure 4a shows the sequential stages of a representative bending and recovery process as recorded using an optical microscope. The bending strain is extracted based on the observed radius of curvature: $\varepsilon_b \approx w/(2R)$, where w is the width of the nanowire and R is the bending radius along the centerline of the nanowire,[38,39] as shown in the upper panel of Figure 4b. The width of the nanowire w is confirmed to be 600 nm using AFM measurement as shown in the lower panel of Figure 4b, which leads to $\varepsilon_b \approx 27.3\%$ with $R \approx 1.1$ μm. The nanowire fully recovers to its initial configuration very quickly (well within 1 s) after being released from this giant strain (>27%). Raman spectra of the SnIP nanowire were measured both before and after this bending strain test at the same bent point. No significant change in the Raman spectra is observed as shown in Figure S4 of the Supporting Information, indicating that there is no noticeable change in the local strain after the recovery. This bending strain is clearly higher than that observed in other semiconducting nanowires.[25,40] The flexibility figure of merit of SnIP is calculated according to $f_{FOM} = \sigma_y/E$, where σ_y is the yield stress,[41] and compared with other materials as shown in Figure 4g. Due to the low E and relatively large σ_y, the f_{FOM} of SnIP is higher than most of not only low-dimensional materials but also polymers. The flexibility (f) of the materials is further related to its thickness (h),[41] $f = (2/h)f_{FOM}$. Thus, once the thickness is narrowed down to the single double helix (~1 nm), the flexibility of SnIP would increase drastically, comparing with current w (~600 nm).

Moreover, more than 20 samples were elastically tested showing a large elastic bending range (7.8−27.3%), and plastic bending was observed when the strain exceeded 29.2%, as shown in Figure 5a. Furthermore, the plastic bending strain can be up to 60% without fracture. We attribute this observation in SnIP to the relatively weak vdW interaction between neighboring double helices in the SnIP crystal, leading to relative slipping between the helices during the bending, which hence results in the large elastic and plastic bending strain. To confirm the vdW interactions between the neighboring double helices in the SnIP crystal, we further calculated the mapping of the charge density and electron

https://doi.org/10.1021/acs.nanolett.2c03394
Nano Lett. 2022, 22, 9054−9061

localization function (ELF) using DFT as shown in Figure 4b, which indicates that the charge density is localized within the helical strands and is much weaker between neighboring double helices units. The slippage energy (E_s) along the [100] direction is calculated to be 0.041 eV/atom. The mirror-symmetrical slipping period is divided into 14 steps to calculate the energy differences (see Figure S5 in the Supporting Information) and 8 of them are shown in Figure 4c. The E_s of SnIP is lower than that of some 2D materials, such as MoS_2 and InSe,[42] indicating a slippery interface along the *a*-axis. Meanwhile, the cleavage energy (E_c) is calculated to be 0.064 eV/atom, which is higher than that of MoS_2 and graphene[42] and higher than the E_s of SnIP. It shows that the SnIP double helices units in the crystal favor slipping (smaller E_s) to release the local strain caused by the bending. Moreover, during the slipping, the double helices are expected to bind tightly together (larger E_c), leading to a larger observed elastic strain than the predicted elastic limit without considering the slipping effect. The slipping between neighboring basal planes has also been experimentally observed during the bending of 2D van der Waals materials such as hexagonal boron nitride,[43] in which the interlayer coupling is also based on vdW interaction similar to the interhelix coupling in SnIP. Furthermore, we adopt the deformability factor proposed in ref 42. $\Xi = (E_c/E_s)(1/E)$ (in units of GPa^{-1}) to evaluate the bendability of the SnIP nanowire. In Figure 4d, the deformability of SnIP crystal is benchmarked with respect to other materials of different bandgaps. Due to the much lower Young's modulus, the deformability of SnIP is the highest among all the known inorganic semiconductors, higher than vdW layered materials such as MoS_2, and InSe,[42] and Ag_2S,[44] and is comparable to ductile metals such as titanium.

This study revealed the ultralow Young's modulus of inorganic double helical crystal SnIP. Such extraordinary mechanical property originates from the unique crystal lattice of this material in which the strong interatomic bonding is tangential to the *a*-axis of the crystal, resulting in an atomic-scale spring-like double helical structure. The large elastic and plastic bending strain are also observed due to the pliability of the double helices and the presence of easy slippage pathways along the *a*-axis, giving rise to a record high flexibility and deformability factor among inorganic semiconductor materials. The ultralow Young's modulus and high elastic bending strain in this unique inorganic semiconductor crystal, combined with its high predicted electron mobility,[45] indicate a promising potential for applications in a broad range of nanomechanical and nanoelectronics disciplines, especially where giant stretchability and bendability are desired.

■ ASSOCIATED CONTENT

Supporting Information

The Supporting Information is available free of charge at https://pubs.acs.org/doi/10.1021/acs.nanolett.2c03394.

Microscopy images, X-ray spectoscopy mapping, displacement distribution results, Raman spectra, free energy during slipping process, and methods (PDF)

■ AUTHOR INFORMATION

Corresponding Authors

Jiangbin Wu − *Ming Hsieh Department of Electrical and Computer Engineering, University of Southern California, Los Angeles, California 90089, United States;* orcid.org/0000-0002-8751-7082; Email: jiangbiw@usc.edu

Han Wang − *Ming Hsieh Department of Electrical and Computer Engineering and Mork Family Department of Chemical Engineering and Materials Science, University of Southern California, Los Angeles, California 90089, United States;* orcid.org/0000-0001-5121-3362; Email: han.wang.4@usc.edu

Authors

Nan Wang − *Mork Family Department of Chemical Engineering and Materials Science, University of Southern California, Los Angeles, California 90089, United States*

Ya-Ru Xie − *State Key Laboratory of Superlattices and Microstructures, Institute of Semiconductors, Chinese Academy of Sciences, Beijing 100083, China*

Hefei Liu − *Ming Hsieh Department of Electrical and Computer Engineering, University of Southern California, Los Angeles, California 90089, United States;* orcid.org/0000-0001-6533-7112

Xinghao Huang − *Department of Aerospace and Mechanical Engineering, University of Southern California, Los Angeles, California 90089, United States*

Xin Cong − *State Key Laboratory of Superlattices and Microstructures, Institute of Semiconductors, Chinese Academy of Sciences, Beijing 100083, China*

Hung-Yu Chen − *Ming Hsieh Department of Electrical and Computer Engineering, University of Southern California, Los Angeles, California 90089, United States*

Jiahui Ma − *Ming Hsieh Department of Electrical and Computer Engineering, University of Southern California, Los Angeles, California 90089, United States*

Fanxin Liu − *Collaborative Innovation Center for Information Technology in Biological and Medical Physics, and College of Science, Zhejiang University of Technology, Hangzhou 310023, P. R. China;* orcid.org/0000-0003-0445-3886

Hangbo Zhao − *Department of Aerospace and Mechanical Engineering, University of Southern California, Los Angeles, California 90089, United States;* orcid.org/0000-0001-5229-4192

Jun Zhang − *State Key Laboratory of Superlattices and Microstructures, Institute of Semiconductors, Chinese Academy of Sciences, Beijing 100083, China;* orcid.org/0000-0002-9831-6796

Ping-Heng Tan − *State Key Laboratory of Superlattices and Microstructures, Institute of Semiconductors, Chinese Academy of Sciences, Beijing 100083, China;* orcid.org/0000-0001-6575-1516

Complete contact information is available at: https://pubs.acs.org/10.1021/acs.nanolett.2c03394

Author Contributions

#J.W. and N.W. contributed equally to this work.

Notes

The authors declare the following competing financial interest(s): H.W. currently also has an appointment with Taiwan Semiconductor Manufacturing Company (TSMC).

■ ACKNOWLEDGMENTS

X.H. acknowledges support from the USC Viterbi Graduate Student Fellowship. H.Z. acknowledges support from the ASME Haythornthwaite Foundation Research Initiation Grant.

REFERENCES

(1) Lee, J.-S.; Kovalenko, M. V.; Huang, J.; Chung, D. S.; Talapin, D. V. Band-like transport, high electron mobility and high photoconductivity in all-inorganic nanocrystal arrays. *Nat. Nanotechnol.* **2011**, *6*, 348−352.

(2) Fang, H.; Zhao, J.; Yu, K. J.; Song, E.; Farimani, A. B.; Chiang, C.-H.; Jin, X.; Xue, Y.; Xu, D.; Du, W.; et al. Ultrathin, transferred layers of thermally grown silicon dioxide as biofluid barriers for biointegrated flexible electronic systems. *Proc. Natl. Acad. Sci. U. S. A.* **2016**, *113*, 11682−11687.

(3) Yu, K. J.; Yan, Z.; Han, M.; Rogers, J. A. Inorganic semiconducting materials for flexible and stretchable electronics. *npj Flexible Electron.* **2017**, *1*, 4.

(4) Yao, J.; Yan, H.; Lieber, C. M. A nanoscale combing technique for the large-scale assembly of highly aligned nanowires. *Nat. Nanotechnol.* **2013**, *8*, 329−335.

(5) Dasgupta, N. P.; Sun, J.; Liu, C.; Brittman, S.; Andrews, S. C.; Lim, J.; Gao, H.; Yan, R.; Yang, P. 25th anniversary article: semiconductor nanowires−synthesis, characterization, and applications. *Adv. Mater.* **2014**, *26*, 2137−2184.

(6) Wu, W.; Wen, X.; Wang, Z. L. Taxel-Addressable Matrix of Vertical-Nanowire Piezotronic Transistors for Active and Adaptive Tactile Imaging. *Science* **2013**, *340*, 952−957.

(7) Khang, D.-Y.; Jiang, H.; Huang, Y.; Rogers, J. A. A Stretchable Form of Single-Crystal Silicon for High-Performance Electronics on Rubber Substrates. *Science* **2006**, *311*, 208−212.

(8) Rogers, J. A.; Someya, T.; Huang, Y. Materials and mechanics for stretchable electronics. *Science* **2010**, *327*, 1603−1607.

(9) Fan, J. A.; Yeo, W.-H.; Su, Y.; Hattori, Y.; Lee, W.; Jung, S.-Y.; Zhang, Y.; Liu, Z.; Cheng, H.; Falgout, L.; Bajema, M.; Coleman, T.; Gregoire, D.; Larsen, R. J.; Huang, Y.; Rogers, J. A. Fractal design concepts for stretchable electronics. *Nat. Commun.* **2014**, *5*, 3266.

(10) Watson, J. D.; Crick, F. H. A structure for deoxyribose nucleic acid. *Nature* **1953**, *171*, 737−738.

(11) Su, D. S. Inorganic Materials with Double-Helix Structures. *Angew. Chem., Int. Ed.* **2011**, *50*, 4747−4750.

(12) Berl, V.; Huc, I.; Khoury, R. G.; Krische, M. J.; Lehn, J.-M. Interconversion of single and double helices formed from synthetic molecular strands. *Nature* **2000**, *407*, 720−723.

(13) Wei, B.; Dai, M.; Yin, P. Complex shapes self-assembled from single-stranded DNA tiles. *Nature* **2012**, *485*, 623−626.

(14) Zhao, M.-Q.; Zhang, Q.; Tian, G.-L.; Wei, F. Emerging double helical nanostructures. *Nanoscale* **2014**, *6*, 9339−9354.

(15) Motojima, S.; Kawaguchi, M.; Nozaki, K.; Iwanaga, H. Growth of regularly coiled carbon filaments by Ni catalyzed pyrolysis of acetylene, and their morphology and extension characteristics. *Appl. Phys. Lett.* **1990**, *56*, 321−323.

(16) Liu, Y.; Wang, J.; Kim, S.; Sun, H.; Yang, F.; Fang, Z.; Tamura, N.; Zhang, R.; Song, X.; Wen, J.; et al. Helical van der Waals crystals with discretized Eshelby twist. *Nature* **2019**, *570*, 358−362.

(17) Zhao, Y.; Zhang, C.; Kohler, D. D.; Scheeler, J. M.; Wright, J. C.; Voyles, P. M.; Jin, S. Supertwisted spirals of layered materials enabled by growth on non-Euclidean surfaces. *Science* **2020**, *370*, 442−445.

(18) Jariwala, D.; Sangwan, V. K.; Lauhon, L. J.; Marks, T. J.; Hersam, M. C. Carbon nanomaterials for electronics, optoelectronics, photovoltaics, and sensing. *Chem. Soc. Rev.* **2013**, *42*, 2824−2860.

(19) Lehn, J.-M.; Rigault, A.; Siegel, J.; Harrowfield, J.; Chevrier, B.; Moras, D. Spontaneous assembly of double-stranded helicates from oligobipyridine ligands and copper (I) cations: structure of an inorganic double helix. *Proc. Natl. Acad. Sci. U. S. A.* **1987**, *84*, 2565−2569.

(20) Soghomonian, V.; Chen, Q.; Haushalter, R. C.; Zubieta, J.; O'Connor, C. J. An inorganic double helix: hydrothermal synthesis, structure, and magnetism of chiral [(CH3) 2NH2] K4 [V10O10 (H2O) 2 (OH) 4 (PO4) 7]· 4H2O. *Science* **1993**, *259*, 1596−1599.

(21) Pfister, D.; Schäfer, K.; Ott, C.; Gerke, B.; Pöttgen, R.; Janka, O.; Baumgartner, M.; Efimova, A.; Hohmann, A.; Schmidt, P.; et al. Inorganic double helices in semiconducting SnIP. *Adv. Mater.* **2016**, *28*, 9783−9791.

(22) Wu, J.; Chen, H.-Y.; Yang, N.; Cao, J.; Yan, X.; Liu, F.; Sun, Q.; Ling, X.; Guo, J.; Wang, H. High tunnelling electroresistance in a ferroelectric van der Waals heterojunction via giant barrier height modulation. *Nat. Electron.* **2020**, *3*, 466−472.

(23) Wu, J.; Cong, X.; Niu, S.; Liu, F.; Zhao, H.; Du, Z.; Ravichandran, J.; Tan, P. H.; Wang, H. Linear Dichroism Conversion in Quasi-1D Perovskite Chalcogenide. *Adv. Mater.* **2019**, *31*, 1902118.

(24) He, M.; Li, Y.; Cai, J.; Liu, Y.; Watanabe, K.; Taniguchi, T.; Xu, X.; Yankowitz, M. Symmetry breaking in twisted double bilayer graphene. *Nat. Phys.* **2021**, *17* (1), 26−30.

(25) Wang, S.; Shan, Z.; Huang, H. The mechanical properties of nanowires. *Adv. Sci.* **2017**, *4*, 1600332.

(26) Wu, B.; Heidelberg, A.; Boland, J. J. Mechanical properties of ultrahigh-strength gold nanowires. *Nat. Mater.* **2005**, *4*, 525−529.

(27) Gere, J. M.; Timoshenko, S.*Mechanics of Materials*; PWS Publishing Company, 1997.

(28) Kresse, G.; Joubert, D. From ultrasoft pseudopotentials to the projector augmented-wave method. *Phys. Rev. B* **1999**, *59*, 1758.

(29) Kresse, G.; Furthmüller, J. Efficient iterative schemes for ab initio total-energy calculations using a plane-wave basis set. *Phys. Rev. B* **1996**, *54*, 11169.

(30) Blöchl, P. E. Projector augmented-wave method. *Phys. Rev. B* **1994**, *50*, 17953.

(31) Cusack, S.; Miller, A. Determination of the elastic constants of collagen by Brillouin light scattering. *J. Mol. Biol.* **1979**, *135*, 39−51.

(32) Gammon, R. W.Examples of Crystal Brillouin Scattering Polarization Selection Rules. In *Light Scattering Spectra of Solids*; Springer, 1969; pp 579−579.

(33) Lai, J.-M.; Xie, Y.-R.; Zhang, J. Detection of electron-phonon coupling in two-dimensional materials by light scattering. *Nano Res.* **2021**, *14* (6), 1711−1733.

(34) Testardi, L.; Hauser, J. Sound velocity in amorphous Ge and Si. *Solid State Commun.* **1977**, *21*, 1039−1041.

(35) Ott, C.; Reiter, F.; Baumgartner, M.; Pielmeier, M.; Vogel, A.; Walke, P.; Burger, S.; Ehrenreich, M.; Kieslich, G.; Daisenberger, D.; et al. Flexible and Ultrasoft Inorganic 1D Semiconductor and Heterostructure Systems Based on SnIP. *Adv. Funct. Mater.* **2019**, *29*, 1900233.

(36) Parker, E. R.*Materials Data Book For Engineers and Scientists*; McGraw-Hill Book Company: New York, 1967.

(37) Tang, D.-M.; Ren, C.-L.; Wang, M.-S.; Wei, X.; Kawamoto, N.; Liu, C.; Bando, Y.; Mitome, M.; Fukata, N.; Golberg, D. Mechanical properties of Si nanowires as revealed by in situ transmission electron microscopy and molecular dynamics simulations. *Nano Lett.* **2012**, *12*, 1898−1904.

(38) Leipholz, U.*Theory of Elasticity*; Springer: Dordrecht, The Netherlands, 1974.

(39) Wang, L.; Zheng, K.; Zhang, Z.; Han, X. Direct atomic-scale imaging about the mechanisms of ultralarge bent straining in Si nanowires. *Nano Lett.* **2011**, *11*, 2382−2385.

(40) Zhang, H.; Tersoff, J.; Xu, S.; Chen, H.; Zhang, Q.; Zhang, K.; Yang, Y.; Lee, C.-S.; Tu, K.-N.; Li, J.; Lu, Y. Approaching the ideal elastic strain limit in silicon nanowires. *Sci. Adv.* **2016**, *2*, e1501382.

(41) Peng, J.; Snyder, G. J. A figure of merit for flexibility. *Science* **2019**, *366*, 690−691.

(42) Wei, T.-R.; Jin, M.; Wang, Y.; Chen, H.; Gao, Z.; Zhao, K.; Qiu, P.; Shan, Z.; Jiang, J.; Li, R.; et al. Exceptional plasticity in the bulk single-crystalline van der Waals semiconductor InSe. *Science* **2020**, *369*, 542−545.

(43) Rooney, A.; Li, Z.; Zhao, W.; Gholinia, A.; Kozikov, A.; Auton, G.; Ding, F.; Gorbachev, R.; Young, R.; Haigh, S. Anomalous twin boundaries in two dimensional materials. *Nat. Commun.* **2018**, *9*, 3597.

(44) Shi, X.; Chen, H.; Hao, F.; Liu, R.; Wang, T.; Qiu, P.; Burkhardt, U.; Grin, Y.; Chen, L. Room-temperature ductile inorganic semiconductor. *Nat. Mater.* **2018**, *17*, 421−426.

https://doi.org/10.1021/acs.nanolett.2c03394
Nano Lett. 2022, 22, 9054−9061

(45) Li, X.; Dai, Y.; Ma, Y.; Li, M.; Yu, L.; Huang, B. Landscape of DNA-like inorganic metal free double helical semiconductors and potential applications in photocatalytic water splitting. *J. Mater. Chem.* **2017**, *5*, 8484−8492.

https://doi.org/10.1021/acs.nanolett.2c03394
Nano Lett. 2022, 22, 9054−9061